Enhancement of superconducting transition temperature and exotic stoichiometries in the Lu-S system under high pressure

Juefei Wu,[1] Bangshuai Zhu,[1] Chi Ding,[2] Dexi Shao,[3] Cuiying Pei,[1] Qi Wang,[1,4] Jian Sun,[2,*] and Yanpeng Qi[1,4,5,†]

[1]*School of Physical Science and Technology, ShanghaiTech University, Shanghai 201210, China*

[2]*National Laboratory of Solid State Microstructures, School of Physics and Collaborative Innovation Center of Advanced Microstructures, Nanjing University, Nanjing 210093, China*

[3]*School of Physics, Hangzhou Normal University, Hangzhou 31121, China*

[4]*ShanghaiTech Laboratory for Topological Physics, ShanghaiTech University, Shanghai 201210, China*

[5]*Shanghai Key Laboratory of High-Resolution Electron Microscopy, ShanghaiTech University, Shanghai 201210, China*

(Received 21 December 2023; revised 22 February 2024; accepted 27 March 2024; published 16 May 2024)

Binary metal sulfides are a potential family of materials for exploring high T_c superconductors under high pressure. In this work, we study the crystal structures, electronic structures, and superconducting properties of the Lu-S system in the pressure range from 0 to 200 GPa, combining crystal structure predictions with *ab initio* calculations. We predict 15 unique structures, encompassing seven unidentified stoichiometries. Within the S-rich structures, the formation of S atom cages is beneficial for superconductivity, with the superconducting transition temperature 25.86 and 25.30 K for LuS_6-$C2/m$ at 70 GPa and LuS_6-R-3m at 90 GPa, respectively. With the Lu/(Lu+S) ratio increases, the Lu-d electrons participate more in the electronic properties at the Fermi energy, resulting in the coexistence of superconductivity and topological nontriviality of LuS_2-$Cmca$, as well as the superconductivity of predicted Lu-rich compounds. Our calculation is helpful for understanding the exotic properties in the transition metal sulfides system under high pressure, providing the possibility of designing alternative superconductors for future experimental and theoretical works.

DOI: 10.1103/PhysRevResearch.6.023177

I. INTRODUCTION

The pursuit for novel superconductors has been an important topic in condensed matter physics. The successful synthesis of H_3S under 155 GPa with the superconducting critical temperature T_c about 203 K [1,2] after theoretical predictions [3,4] has accelerated the research on hydrogen metallization by "chemical precompression" from other elements [5], such as the binary hydrides with clathrate structures, CaH_6, YH_9, LaH_{10}, etc. [6–13]. Meanwhile, Ref. [14] proposed that one can also look for breakthroughs in new classes of compounds, such as borides [15–19], lithium-rich compounds [20–23], sulfides, etc.

The simple substance sulfur is superconducting under high pressure, with T_c about 15 K at 100 GPa [24]. In addition, the T_c has the potential to reach about 17 K above 157 GPa [25] or 17.3 K at 200 GPa [26] by ac magnetic susceptibility measurements. The T_c value of sulfur is the highest among the nonmetal elements except for hydrogen [27], and the metallization condition is less confined than hydrogen, indicating promising prospects in novel structure designing. As concluded in Ref. [28], it is tough for the T_c values of the binary metal sulfides to exceed 5 K at ambient condition, with the 2M-WS_2 reaching 8.8 K [29]. Nevertheless, the T_c values of MoS_2 and 2H-TaS_2 are above 10 K under high pressure, which are 12 K at 200 GPa [30] and 16.4 K at 157.4 GPa [31], respectively. Zhang *et al.* found that the superconducting state of PbS can be around 12 K at 19 GPa, which lowers the synthesized pressure from 1 Mbar [28]. In the aspect of theoretical studies, Gonzalez *et al.* explored the Sn-S system and predicted two superconducting structures; the T_c values are 9.74 and 21.9 K for SnS-Pm-3m at 40 GPa and Sn_3S_4-I-42d at 30 GPa, respectively [32]. Thereafter, Matsumoto *et al.* confirmed the pressure induced superconductivity of SnS-Pm-3m [33]. Additionally, Shao *et al.* proposed the exotic compound Al_3S_4-I-43d, which has a T_c value of 20.9 K at 100 GPa [34].

The transition metal could provide chemical pressure and lower the metallization pressure of hydrogen, supporting the high T_c values of binary hydrides like YH_9 and LaH_{10}. This inspires the predictions in transition metal sulfides under high pressure. The high pressure synthesized Y_3S_4-I-43d shows weak superconductivity (3.6 K) [35], while Chen *et al.* predicted an unconventional stoichiometric YS_3-Pm-3, which is 18.5 K at 50 GPa [36]. Gao *et al.* predicted superconducting S-rich lanthanum sulfides under high pressure; the S cages stacked LaS_3 and LaS_5 are superconductors with a T_c of 13.6 K at 100 GPa and 11 K at 120 GPa, respectively [37]. Comparing with Al-S and Sn-S systems, transition metals have the potential to elevate the S atom ratio in binary metal

*jiansun@nju.edu.cn
†qiyp@shanghaitech.edu.cn

sulfides with exotic structures. Since the last lanthanide element lutetium has similarities to lanthanum, which has the same unoccupied $5d$ orbitals accompanied with a full $4f$ shell, we wonder whether Lu can further improve the S atom ratio in metal sulfides and enrich the binary sulfides family. Thus it could be intriguing to explore the unique structures and exotic properties of the Lu-S system under high pressure.

In this work, we focus on exploring the Lu-S binary metal sulfides within 200 GPa, combining the machine learning graph theory accelerated crystal structure search with first-principles calculations. We predict 15 unique structures and seven alternative stoichiometries in the Lu-S system. There are potential superconductors in LuS_7, LuS_6, LuS_3, LuS_2, Lu_5S_3, Lu_2S, and Lu_3S under high pressure. The T_c values of the metastable LuS_6-$C2/m$ and LuS_6-$R\text{-}3m$ are about 25 K under high pressure, and we find the coexistence of superconductivity and topological nontriviality in LuS_2-$Cmca$ under high pressure. Combined with the calculations of the electronic structures and electron-phonon coupling (EPC) properties, we find that Lu-d electrons are more involved in the electronic properties with the increasing of the Lu/(Lu+S) ratio, which alters the mechanism of superconductivity from the S-rich compounds to Lu-rich compounds.

II. METHODS

We use the machine learning graph theory accelerated crystal structure search method (MAGUS) [38,39] to perform the variable composition structure searches for lutetium sulfides under 50, 100, 150, and 200 GPa, respectively. Then we carry out structure searches for the specific compositions, with more than 1000 structures evolved in 30 generations. Within MAGUS runs, we combine the Vienna *ab initio* simulation package (VASP) based on the density functional theory [40,41] to perform the structure relaxations. The exchange-correlation functional is treated by the generalized gradient approximation of Perdew, Burke, and Ernzerhof [42], and the projector-augmented wave (PAW) approach [43] is used to describe Lu and S atoms with valence $5s^2\,5p^6\,4f^{14}\,5d^1\,6s^2$ and $3s^2\,3p^4$. The maximum cutoff energy of the plane-wave is set to 400 eV and the sampling grid spacing of the Brillouin zone is $2\pi \times 0.05\,\text{Å}^{-1}$ for structure searches.

We recalculate the enthalpy of the predicted structures to establish the convex hull using VASP. The convergence criteria are enhanced with the plane-wave kinetic-energy cutoff set to 600 eV after testing, and the Brillouin zone sampling resolution is $2\pi \times 0.03\,\text{Å}^{-1}$. The convergence tolerance is 10^{-6} eV for total energy and $0.003\,\text{eV/Å}$ for all forces. The electronic structure calculations uses a denser k-mesh grid of $2\pi \times 0.02\,\text{Å}^{-1}$ and the total energy is converged to be less than 10^{-8} eV. The aforementioned convergence threshold is for the entire simulation cell. The cell parameters are in Table S1 in the Supplemental Material [44] and the structure marked with an asterisk indicates the primitive cell is used for enthalpy calculations. We construct tight-binding models based on maximally localized Wannier functions (MLWFs) using WANNIER90 code [45]. The topological electronic structures are studied by the WANNIERTOOLS package [46].

The phonon spectra are calculated by the PHONOPY [47] program package using the finite displacement method combined with VASP. The supercell is $2 \times 2 \times 2$ for all the candidate structures. We use the relaxed structure in VASP to perform the EPC coefficients calculations by the QUANTUM ESPRESSO (QE) package [48] using density functional perturbation theory [49] without the re-relaxing by QE. We select the ultrasoft pseudopotential with a kinetic-energy cutoff of 70 Ry after testing; the details of the k mesh and q mesh for different structures are in Table S2 [44]. The Marzari–Vanderbilt–De Vita–Payne cold smearing is taken into account in the self-consistency calculations and electron-phonon is calculated by interpolation over the Brillouin zone. To estimate the superconducting transition temperature T_c of the predicted structures, we use the Allen-Dynes modified McMillan formula [50],

$$T_c = \frac{\omega_{\log}}{1.2}\exp\left[\frac{-1.04(1+\lambda)}{\lambda-\mu^*(1+0.62\lambda)}\right], \tag{1}$$

where $\omega_{\log}$ is the logarithmic average frequency. As reported in Ref. [11], current harmonic approximation may neglect the potential anharmonic effects of the light element compounds under high pressure, and the commonly used Coulomb pseudopotential μ^* value may overestimate the T_c value. Thus we choose the μ^* value 0.1–0.15 to give the estimated T_c value and we expect to provide more experimental evidence and look further into the anharmonic effects in future works. The EPC constant λ and $\omega_{\log}$ are defined as follows:

$$\lambda = 2\int_0^\infty \frac{\alpha^2F(\omega)}{\omega}\,\mathrm{d}\omega, \tag{2}$$

and

$$\omega_{\log} = \exp\left[\frac{2}{\lambda}\int\frac{\mathrm{d}\omega}{\omega}\alpha^2F(\omega)\ln(\omega)\right]. \tag{3}$$

III. RESULTS AND DISCUSSION

To investigate the stable phases in the Lu-S system under high pressure, we calculate the formation enthalpies of all the predicted structures by the variable composition structure searches under 50, 100, 150, and 200 GPa, and construct the convex hull diagrams in intervals of 20 GPa. As shown in Fig. 1, we select the simple substances Lu and S [51–55] under corresponding pressures as the references. At ambient pressure, only the known compounds in LuS and Lu_2S_3 are on the convex hull. Above 20 GPa, other stoichiometries emerge and they approach the convex hull with the increasing of pressure. The predicted stoichiometries LuS_3, LuS_2 and Lu_5S_3 lie on the convex hull at 60 GPa. Upon further compression, the predicted stoichiometries Lu_2S and Lu_3S are less than 50 meV/atom above the convex hull. Lu_2S and Lu_3S lie on the convex hull at 200 and 180 GPa, respectively. Despite the predicted stoichiometries LuS_6 and LuS_7 are not on the convex hull within 200 GPa; LuS_6 is 35 meV/atom above the convex hull and LuS_7 is 42 meV/atom from the convex hull at 80 GPa, indicating their metastability under high pressure.

Combining the detailed calculations of relative enthalpy difference in each composition under high pressure (Fig. S1) [44], we summarize the pressure composition phase diagram for the Lu-S system in Fig. 2. We take the threshold of 50 meV/atom to estimate the metastable state, which is common in structure predictions [56]. Our calculations re-

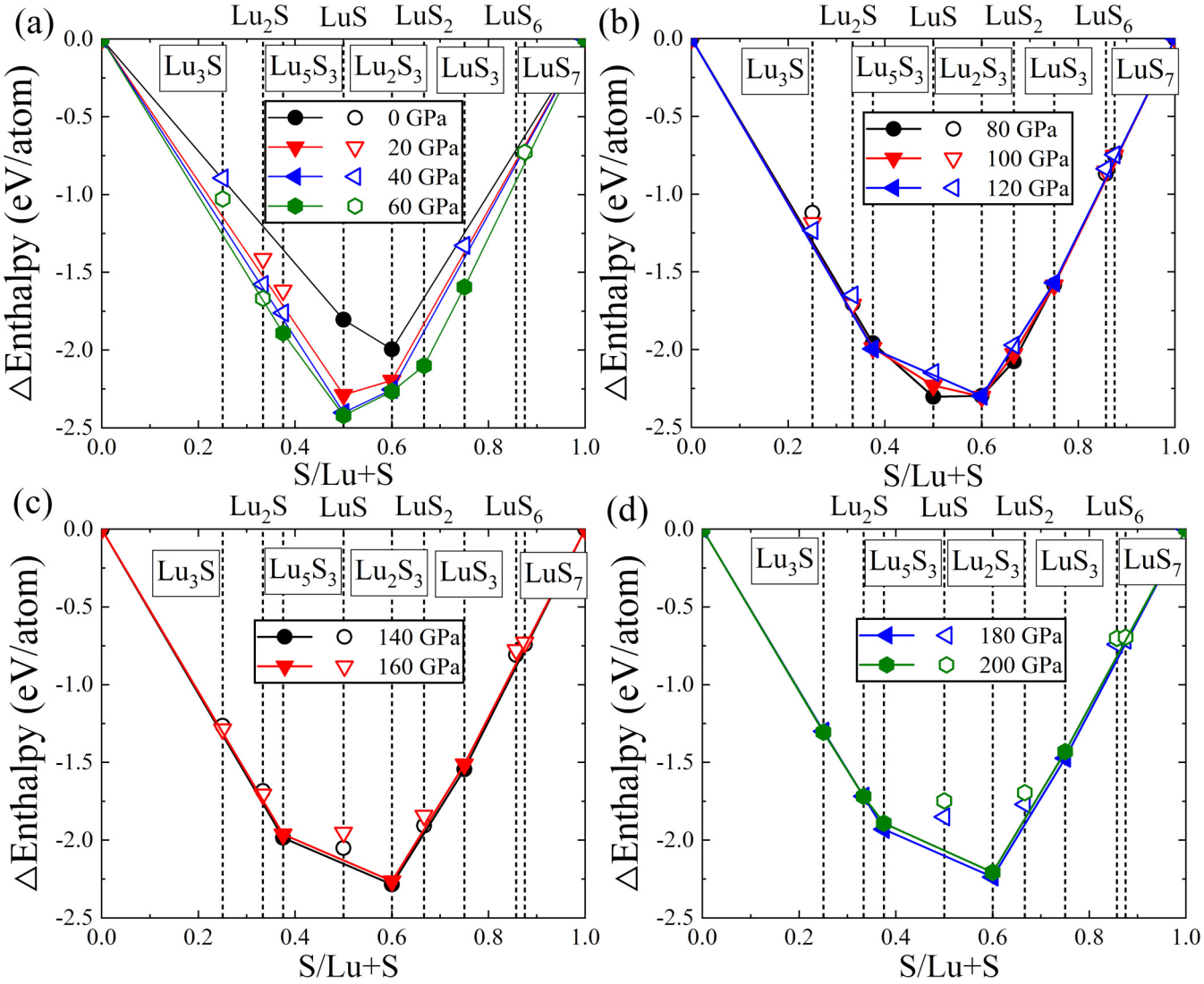

FIG. 1. The convex hull diagrams for Lu-S binary compounds under high pressures. The solid points indicate that the stoichiometries are on the convex hull, while the empty points are above the convex hull.

produce the stability of the reported structures LuS-*R*-3c and Lu_2S_3-*Fm*-3*m* at ambient condition and predict 15 unique structures LuS_7-*R*-3, LuS_6-*C*2/*m*, LuS_6-*R*-3*m*, LuS_3-*Pm*-3*n*, LuS_3-*P*2$_1$/*m*, LuS_3-*Cmcm*, LuS_2-*Cmca*, Lu_2S_3-*P*4/*mbm*, Lu_2S_3-*I*4/*mmm*, LuS-*Pm*-3*m*, Lu_5S_3-*C*2/*m*, Lu_5S_3-*P*6$_3$/*mcm*, Lu_2S-*Cmcm*, Lu_2S-*P*6$_3$/*mmc*, and Lu_3S-*Imma* within nine stoichiometries (Fig. 2); the detailed lattice parameters and atomic coordinates are listed in Table S1 [44]. The phonon spectra of the predicted structures are in Figs. S2–S5 [44]. The absence of imaginary frequencies in the whole Brillouin zone illustrates their dynamical stability within the calculated pressure range. Additionally, we perform the spin-polarized calculations in all the predicted structures; none of them are magnetic within 200 GPa.

As depicted in Fig. 2, the predicted LuS_7-*R*-3 structure is metastable from 74 GPa. Its relative enthalpy difference between the convex hull is decreasing with pressure, which is around 20 meV/atom at 200 GPa [Fig. S1(a)] [44]. The crystal structure of LuS_7-*R*-3 is shown in Fig. 3(a); S atoms surround the Lu atom forming S_{12} cages [Fig. 3(b)]. The labeled S atom has a little shift and causes the distortion of the S_{12} cages, which has a discrepancy with the LaS_{12} cages [37]. These cages stack with each other constituting the LuS_7-*R*-3 structure. The phonon spectrum indicates that the LuS_7-*R*-3 structure can keep dynamical stability at 50 GPa [Fig. S2(a)] [44]. We further calculate the band structures and the partial density of states (PDOS) at 50 GPa [Fig. S6(a)] [44]. The *p* electrons of the S atoms make the main contribution in the range of −3 to 3 eV. The peaks in PDOS around the Fermi energy may be beneficial for superconductivity. The electron localization function (ELF) results crossing the Lu-S_4 plane of the S_{12} cages are shown in Fig. 3(c). There is almost no local charge between Lu and S atoms, suggesting ionic bonding properties, while the ELF between S atoms indicates covalent bonding and forms the S-S channel between S_{12} cages. Then we carry out calculations on EPC constants, the projected phonon density of states (PHDOS), the Eliashberg spectral function $\alpha^2F(\omega)$, and the electron-phonon integral $\lambda(\omega)$ [Fig. 3(d)]. The vibration frequencies above 100 cm^{-1} play a dominant role in EPC, which corresponds to S atoms

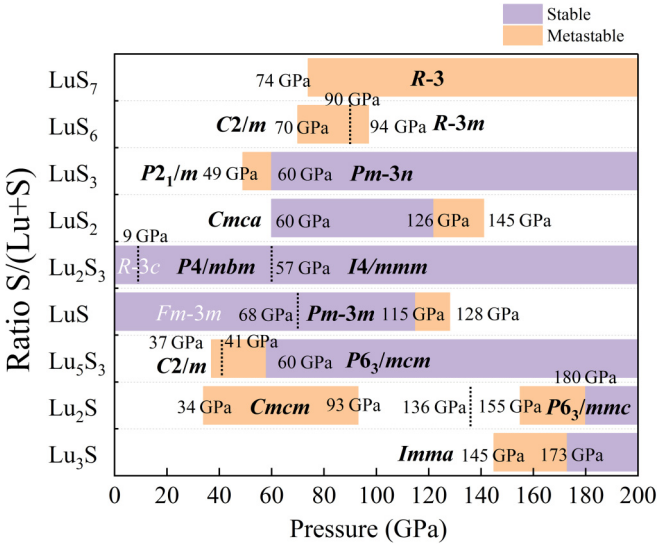

FIG. 2. The pressure-composition phase diagram of the Lu-S binary compounds. The predicted structures are in black bold font, while the reported structures are in white font. The violet region indicates the thermodynamically stable state and the orange region is the metastable state. The dashed lines are the boundary between different phases in each stoichiometry.

in the aspect of PHDOS. Hence the S_{12} cages could be the key factor to the superconductivity in LuS_7-R-3. The calculated EPC constant λ is 0.98 and the T_c estimated by the Allen-Dynes modified McMillan formula reaches around 13.15–17.43 K (Table I)].

We predict two metastable structures LuS_6-$C2/m$ and LuS_6-R-3m in LuS_6; both of them consist of S_{12} cages as LuS_7-R-3. As plotted in the inset of Fig. S1(b) [44], the relative enthalpy difference between LuS_6-$C2/m$ and LuS_6-R-3m

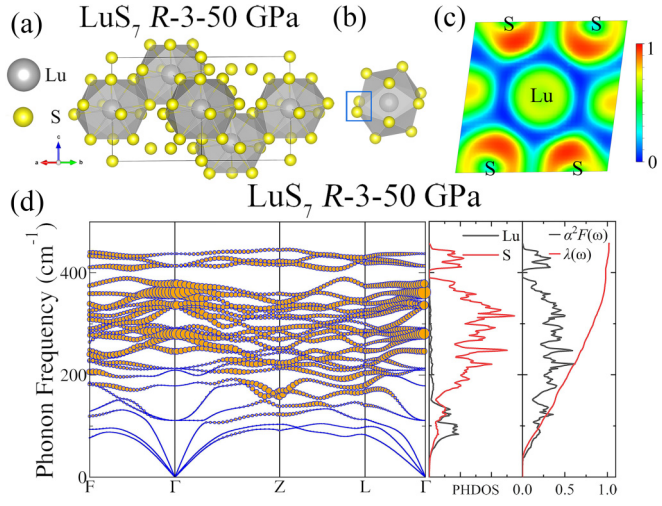

FIG. 3. (a) The crystal structure of LuS_7-R-3 at 50 GPa. (b) The S_{12} cage of LuS_7-R-3. (c) The ELF of LuS_7-R-3. (d) The calculated phonon curves, PHDOS, Eliashberg spectral function $\alpha^2F(\omega)$, and the electron-phonon integral $\lambda(\omega)$ of LuS_7-R-3 under 50 GPa. The orange solid dots represent the phonon linewidth with the radii proportional to the strength.

TABLE I. The calculated superconducting properties of the predicted Lu-S structures under high pressure with μ^* being 0.10–0.15.

Phase	Space group	Pressure (GPa)	λ	T_c (K) $\mu^* = 0.1$	T_c (K) $\mu^* = 0.15$
LuS_7	R-3	50	0.98	17.43	13.15
LuS_6	$C2/m$	70	1.63	25.86	22.37
	R-3m	90	1.11	25.32	20.05
LuS_3	$P2_1/m$	40	0.76	11.02	7.30
	$Cmcm$	70	0.52	4.40	1.92
	Pm-3n	60	0.69	9.57	5.92
LuS_2	$Cmca$	60	0.90	9.10	6.68
Lu_5S_3	$C2/m$	30	0.43	1.11	0.300
Lu_2S	$P6_3/mmc$	100	0.61	4.84	2.68
Lu_3S	$Imma$	100	0.70	6.59	4.14

is less than 5 meV/atom above 60 GPa, which approaches our convergence limitation. Thus we analyze the lattice parameters a, c, α, and γ of LuS_6-$C2/m$ under high pressures [Fig. 4(b)]. After structure optimization, the curves of lattice parameters a and c merge with each other after 90 GPa and their difference is less than 0.1%, which is analogous to that between α and γ. We can observe a small alignment change of the S atoms in the S_{12} cage after 90 GPa [inset of Fig. 4(b)]. From the aspect of symmetry analysis, $C2/m$ could be the *translationengleiche* subgroup or t subgroup of R-3m, i.e., the translation symmetries in the supergroup R-3m are retained and the order of the point group is reduced. In LuS_6, the pressure acts as perturbations in the transition between R-3m and $C2/m$, indicating that the lattice parameters and atomic positions within the primitive cell of R-3m and $C2/m$ have minor evolution near the critical pressure. As shown in Fig. S10 [44], the distinction between the primitive cells of LuS_6-$C2/m$ and LuS_6-R-3m lies in the lengths and angles of the lattice parameters. Hence we illustrate the structure transition by plotting the sublattice of Lu atoms in LuS_6-$C2/m$ and LuS_6-R-3m (Table S1) [44] under high pressure in Fig. S10 [44]. There are two sites of Lu atoms in LuS_6-$C2/m$, (0.00 0.00 0.00) and (0.50 0.50 0.00). We measure the distances and angles between Lu atoms at (0.50 0.50 0.00) and its first nearest Lu atoms. As depicted in Fig. S10(a) [44], a equals Å comparing with c, and α equals β with a difference of 2.05° comparing with γ. If the small distinction in both the distances and angles disappears in the $C2/m$ phase, it will become the R-3m phase with $a = b = c$ and $\alpha = \beta = \gamma$ [Fig. S10(b)] [44]. Thus we assume that the pressure acts as the perturbation in the structure transition between LuS_6-$C2/m$ and LuS_6-R-3m.

In addition, the phonon spectrum calculations [Figs. S2(c)–S2(e)] [44] illustrate that the dynamical stability of LuS_6-$C2/m$ and LuS_6-R-3m is from 70 to 90 GPa, respectively, and we calculate their band structures, PDOS [Figs. S6(b) and S6(c)] [44], and ELF [Fig. 4(c)] under corresponding pressures. Analogous to LuS_7-R-3, the S-p electrons make the main contribution around the Fermi energy, with ionic bonding between Lu and S and covalent bonding between S and S. From the aspect of PHDOS, $\alpha^2F(\omega)$ and $\lambda(\omega)$ of LuS_6-$C2/m$ and LuS_6-R-3m in Figs. 4(d) and 4(e),

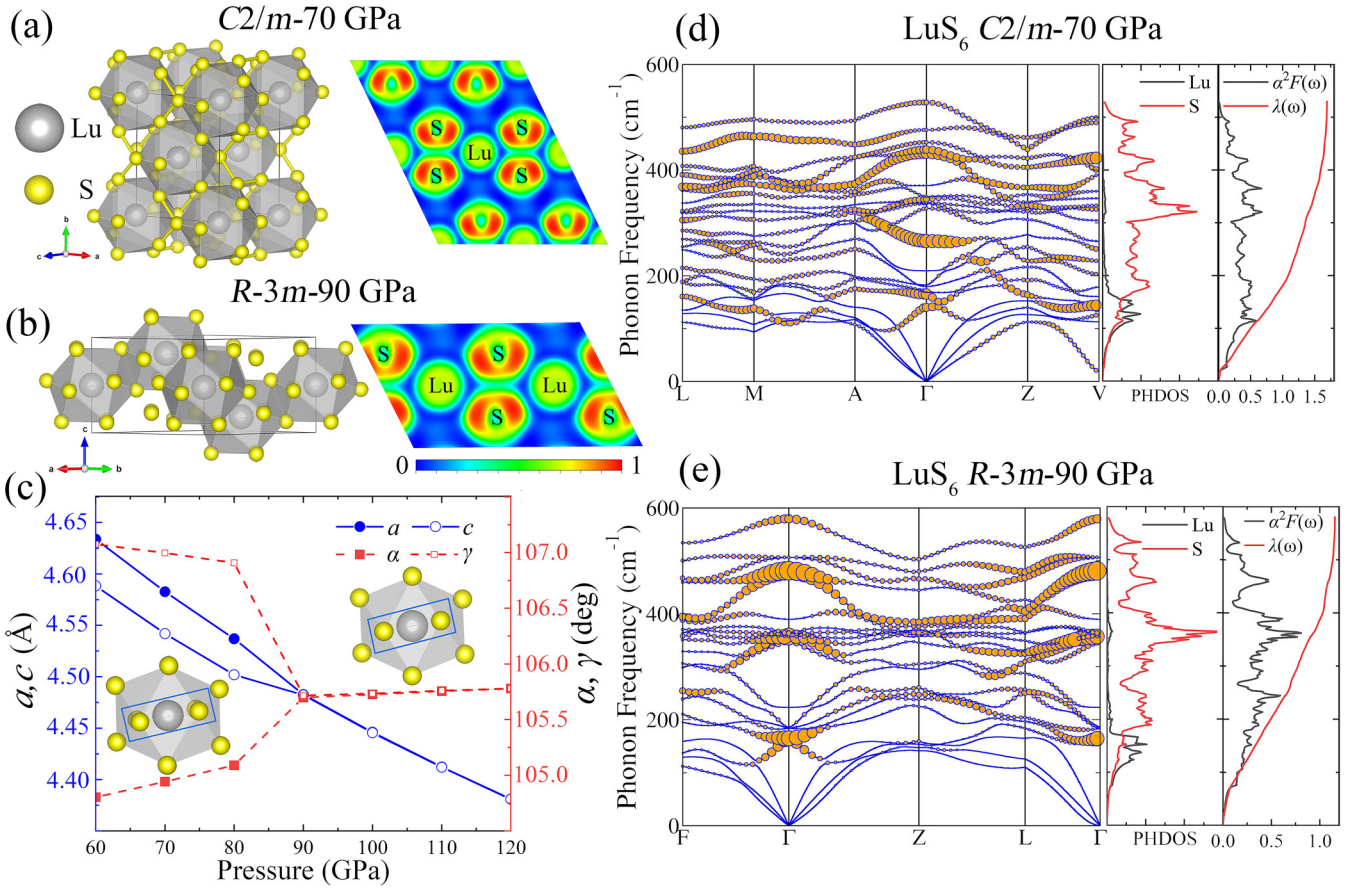

FIG. 4. (a), (b) The crystal structure and corresponding ELF of LuS_6-$C2/m$ and LuS_6-R-$3m$ under high pressures. (c) The lattice parameters a, c, α, and γ of LuS_6-$C2/m$ in relation to pressure; the inset is the S_{12} cage. (d), (e) are the calculated phonon curves, PHDOS, Eliashberg spectral function $\alpha^2F(\omega)$, and the electron-phonon integral $\lambda(\omega)$ of LuS_6-$C2/m$ at 70 GPa and LuS_6-R-$3m$ at 90 GPa, respectively. The orange solid dots represent the phonon linewidth with the radii proportional to the strength.

the dominant contribution to EPC is from S atoms above the 100 cm^{-1} frequency region as well. This provides further evidence that S_{12} cages are crucial to the superconductivity of the caged Lu-S structures. The calculated EPC constants λ are 1.63 and 1.11, and the estimated T_c are around 22.37–25.86 K and 20.05–25.32 K for LuS_6-$C2/m$ at 70 GPa and LuS_6-R-$3m$ at 90 GPa (Table I), respectively. To our knowledge, these estimated T_c values improve the prediction record in the binary transition metal sulfides [28,35,36,57].

There are three predicted structures, $P2_1/m$, Pm-$3n$, and $Cmcm$, in LuS_3. Their relative enthalpies under high pressure are shown in Fig. S1(c) [44]. Despite LuS_3-$Cmcm$ having the lowest enthalpy among three structures below 71 GPa, the phonon spectrum calculations suggest the dynamical stability range of LuS_3-$Cmcm$ is above 70 GPa, which is above 60 GPa for LuS_3-Pm-$3n$ [Figs. S3(a)–S3(d)] [44]. In comparison, the dynamical stability pressure of $P2_1/m$ is from 40 GPa [Figs. S3(g) and S3(h)] [44], and it becomes metastable after 49 GPa from the aspect of enthalpy [inset of Fig. S1(c)] [44]. Hence LuS_3-$P2_1/m$ and LuS_3-$Cmcm$ are metastable, while LuS_3-Pm-$3n$ is stable under high pressure. The crystal structures of the three predicted structures are shown in Figs. 5(a)–5(c). LuS_3-$P2_1/m$ contains distorted S_{12} cages, while LuS_3-Pm-$3n$ is composed of S_{12} cages without distortion as in the La-S system [37]. The ELF of $P2_1/m$ and Pm-$3n$ [Figs. 5(a) and 5(b)] suggests Lu-S is ionic bonding and S-S is covalent bonding. LuS_3-$Cmcm$ is constructed by layers and the S atoms make up the layer boundary. We calculate the ELF of the intra- and interlayer in LuS_3-$Cmcm$ [Fig. 5(c)]. The intralayer is S-S covalent bonding and forms channels, while the connection type between interlayers is ionic. The band structures and PDOS of the three predicted structures [Figs. S7(a)–S7(c)] [44] suggest the main role of the S-p electrons around the Fermi energy. Meanwhile, we can observe the distribution from the electrons of the Lu atoms, which are also reflected in the EPC calculations. As shown in Figs. 5(d)–5(f), the dominant contribution to the EPC constants is from the vibration above ~200 cm^{-1}, which corresponds to S atoms in PHDOS, while the contribution to the integral $\lambda(\omega)$ is larger than 40% in the Lu atom region below ~200 cm^{-1}, particularly in LuS_3-Pm-$3n$ and LuS_3-$Cmcm$ [Figs. 5(e) and 5(f)]. This implies that the electrons of the Lu atoms begin to have an impact on the superconductivity with the increasing of the Lu/(Lu+S) ratio. The EPC constants λ are 0.76, 0.69, and 0.52, with corresponding T_c values of 7.30–11.2 K, 5.92–9.57 K, and 1.92–4.40 K for LuS_3-$P2_1/m$ at 40 GPa, LuS_3-Pm-$3n$ at 60 GPa, and LuS_3-$Cmcm$ at 70 GPa, respectively (Table I). Comparing these T_c values, we assume that the caged structure is more favorable for superconductivity than the layered structure in LuS_3.

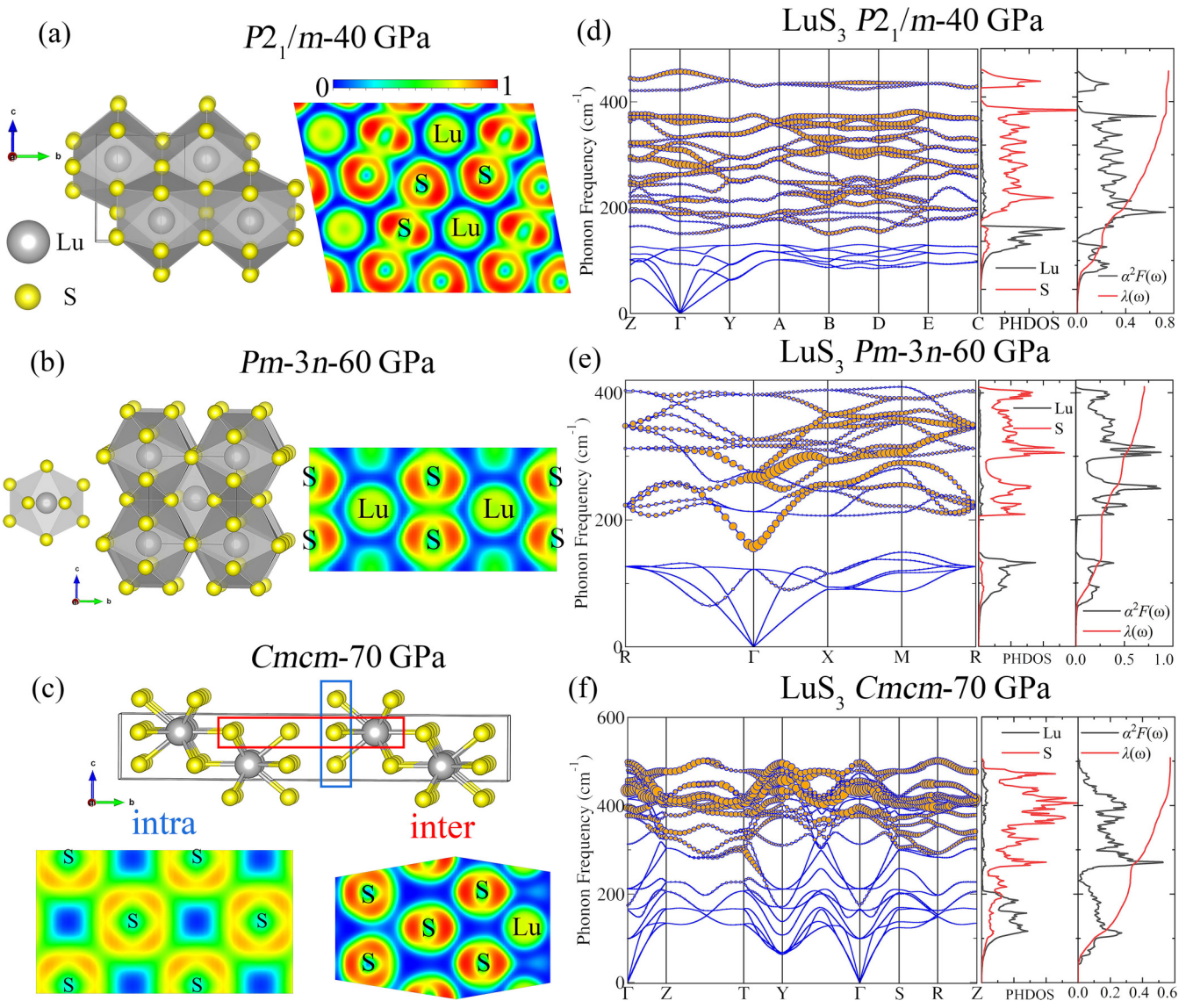

FIG. 5. (a)–(c) The crystal structure and ELF of LuS_3-$P2_1/m$, LuS_3-Pm-3n, and LuS_3-Cmcm under high pressures. (d)–(f) The calculated phonon curves, PHDOS, Eliashberg spectral function $\alpha^2F(\omega)$, and the electron-phonon integral $\lambda(\omega)$ of LuS_3-Pm-3n at 60 GPa and LuS_3-$Cmcm$ at 70 GPa. The orange solid dots represent the phonon linewidth with the radii proportional to the strength.

The predicted structure LuS_2-$Cmca$ contains S_9 cages [Fig. 6(a)]; this is isostructural to LaS_2-$Cmce$ [37]. LuS_2-$Cmca$ transforms to the metastable state after 126 GPa [Fig. 1(d)] and is dynamically stable from 60 GPa [Figs. S3(e) and S3(f)] [44]. The ELF results in different planes suggest the channel between the S_2 dimer and weak bonding between Lu-S [Fig. 6(b)]. In particular, we can observe band nodes on the Fermi energy along the Brillouin paths Γ-S and T-Y-Γ-S, and the bands contain different components S-p and Lu-d, respectively. This is in line with PDOS results that the distribution of Lu-d is comparable to S-p around the Fermi energy, suggesting that electrons of Lu atoms participate more in the electronic properties in LuS_2 than the above predicted S-rich Lu-S compounds. Thereafter, we calculate the $\mathbb{Z}_2$ invariant with the spin-orbital coupling (SOC) for LuS_2-$Cmca$ at 60 GPa. The $\mathbb{Z}_2$ index $(\upsilon_0;\upsilon_1\upsilon_2\upsilon_3) = (1;000)$, suggesting that LuS_2-$Cmca$ is topologically nontrivial at 60 GPa. The surface states on the (001) plane are in Fig. 6(c); we can observe surface states around the S point and along the Y-Γ path. Moreover, we calculated the EPC properties of LuS_2-$Cmca$ at 60 GPa in Fig. 6(c); the Lu atoms contribute about 70% in the integral $\lambda(\omega)$. This is in agreement with PDOS results and Lu atoms are more involved in the electronic properties of LuS_2. The calculated λ is 0.94 and the T_c is 6.68–9.10 K at 60 GPa (Table I). The coexistence of superconductivity and nontriviality in LuS_2-$Cmca$ provides a potential platform for studying the relation between alternative properties.

Lu_2S_3 and LuS are the two stoichiometries with ambient pressure structures [58,59]. In Fig. S1(e) [44], the ambient phase Lu_2S_3-R-3c transforms to the predicted Lu_2S_3-$P4/mbm$ around 9 GPa, then transforms to Lu_2S_3-$I4/mmm$ after 57 GPa. Meanwhile, the ambient LuS-Fm-3m transforms to LuS-Pm-3m above 68 GPa, which becomes metastable about 115 GPa [Fig. S1(f)] [44]. This is in line with the calculations in Ref. [60]. Among the predicted structures in Lu_2S_3 and LuS

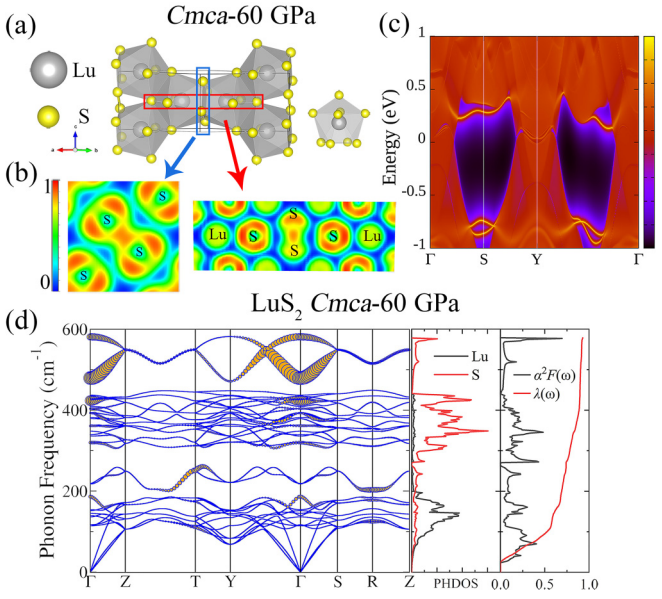

FIG. 6. (a) The crystal structure of LuS_2-*Cmca* at 60 GPa. (b) The ELF of the S atoms plane and S-Lu-S plane. (c) The surface state of LuS_2-*Cmca* at 60 GPa. (d) The calculated phonon curves, PHDOS, the Eliashberg spectral function $\alpha^2F(\omega)$, and the electron-phonon integral $\lambda(\omega)$ of LuS_2-*Cmca* at 60 GPa. The orange solid dots represent the phonon line width with the radii proportional to the strength.

[Figs. 7(a)–7(c)], LuS-*Pm*-3*m* could keep dynamical stability at ambient pressure (Fig. S4) [44]. According to the ELF depicted in Figs. 7(d)–7(f), ionic bonding is predominant, indicating that Lu and S atoms are more isolated than other predicted S-rich compounds. The band structures and PDOS results of Lu_2S_3-*P*4/*mbm*, Lu_2S_3-*I*4/*mmm*, and LuS-*Pm*-3*m* are in Fig. S8 [44]. In the predicted Lu_2S_3 structures, Lu-*d* and S-*p* have similar contributions around the Fermi energy. Lu-*d* and S-*p* are more distributed in conduction bands and valence bands, respectively. Considering the band crossings around the Fermi energy, we calculate the $\mathbb{Z}_2$ invariant and the index $(\upsilon_0;\ \upsilon_1\upsilon_2\upsilon_3) = (0;\ 000)$ for Lu_2S_3-*P*4/*mbm* and Lu_2S_3-*I*4/*mmm*, illustrating that the band structures are topologically trivial. Nevertheless, Lu-*d* becomes dominant in LuS-*Pm*-3*m* with a PDOS peak at Fermi energy, suggesting the growing impact of Lu-*d* with the further increase of Lu/(Lu+S) ratio.

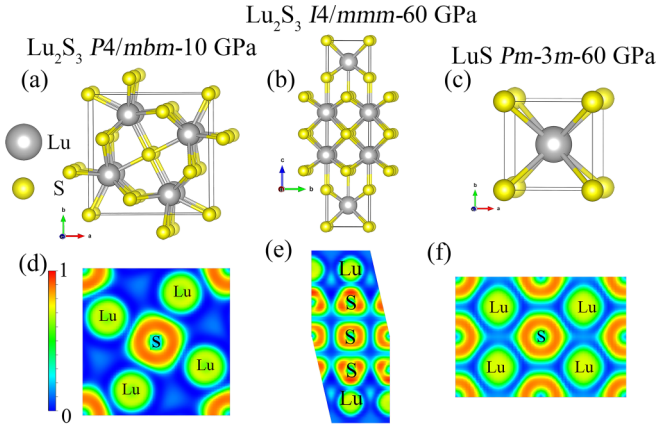

FIG. 7. (a)–(c) The crystal structures of Lu_2S_3-*P*4/*mbm*, Lu_2S_3-*I*4/*mmm*, and LuS-*Pm*-3*m* under high pressures. (d)–(f) The ELF of the corresponding structures.

As for the Lu-rich compounds in the Lu-S system, we predict five unique structures, Lu_5S_3-*C*2/*m*, Lu_5S_3-$P6_3/mcm$, Lu_2S-*Cmcm*, Lu_2S-$P6_3/mmc$, and Lu_3S-*Imma* in three alternative stoichiometries [Figs. 8(a)–8(e)]. The Lu_5S_3-*C*2/*m* has lower enthalpy than Lu_5S_3-$P6_3/mcm$ above 41 GPa [Fig. S1(g)] [44]. Although Lu_5S_3-*C*2/*m* is 50 meV/atom above the convex hull below 37 GPa (Fig. 2), Lu_5S_3-*C*2/*m* is dynamically stable from 30 GPa [Fig. S5(a)] [44], and the pressure for Lu_5S_3-$P6_3/mcm$ is 20 GPa [Fig. S5(c)] [44]. In Lu_2S [Fig. S1(h)] [44], Lu_2S-$P6_3/mmc$ is more thermodynamically stable than Lu_2S-*Cmcm* above 136 GPa, and the modification of the convex hull by Lu_5S_3-$P6_3/mcm$ separates the metastable region into two areas (Fig. 2). Phonon spectra results illustrate that the stabilized pressures start from 20 and 100 GPa for Lu_2S-*Cmcm* and Lu_2S-$P6_3/mmc$ [Figs. S5(g) and S5(i)] [44], respectively. In addition, the predicted Lu_3S-*Imma* is dynamically stable after 100 GPa [Fig. S5(e)] [44], while it enters the metastable region above 145 GPa and becomes stable above 173 GPa [Fig. S1(i)] [44]. The band structures and PDOS of Lu_5S_3-*C*2/*m*, Lu_5S_3-$P6_3/mcm$, Lu_2S-*Cmcm*, Lu_2S-$P6_3/mmc$, and Lu_3S-*Imma* under high pressures are shown in Fig. S9 [44]. In all the five band structures, the Lu-*d* electrons are predominant in the range of −3 to 3 eV. The valence bands and conduction bands overlap with each other around the Fermi energy, illustrating typical metal characteristics. Thus we assume that the itinerant Lu-*d* electrons give rise to the metallicity of Lu_5S_3-*C*2/*m*, Lu_5S_3-$P6_3/mcm$, Lu_2S-*Cmcm*, Lu_2S-$P6_3/mmc$, and Lu_3S-*Imma*, which forms the connection between the S atoms [the ELF in Figs. 8(a)–8(e)] and avoids the isolation in Lu_2S_3 and LuS. Moreover, we calculated the EPC properties of the five predicted structures. Among them, the predicted Lu_5S_3-*C*2/*m*, Lu_2S-$P6_3/mmc$, and Lu_3S-*Imma* are superconducting under high pressure, as depicted in Figs. 8(f)–8(h). Even though the vibration of S atoms make a clear contribution to EPC, more than 80% of the contribution of the integral $\lambda(\omega)$ is from Lu atoms. This illustrates that the coupling between the S atoms and Lu-*d* electrons is the elemental factor for superconductivity in the Lu-rich compounds, which is in agreement with the metallicity induced by Lu-*d* electrons. The EPC constants are 0.43, 0.61, and 0.73 for Lu_5S_3-*C*2/*m* at 30 GPa, Lu_2S-$P6_3/mmc$ at 100 GPa, and Lu_3S-*Imma* at 100 GPa, and the corresponding T_c's are 0.30–1.11 K, 2.68–4.84 K, and 4.14–6.59 K, respectively.

We summarized the calculated EPC constants and the estimated T_c values of the superconducting Lu-S compounds in Table I. The T_c values of the S-rich compounds are relatively higher than the Lu-rich compounds except for the layered LuS_3-*Cmcm*, indicating that the S cages are beneficial for the enhancement of superconductivity in Lu-S systems, such as the caged structures LuS_7-*R*-3, LuS_6-*C*2/*m*, LuS_6-*R*-3*m*, and LuS_3-*Pm*-3*n*. With the increasing of the Lu/(Lu+S) ratio, Lu-*d* electrons are involved more in the electronic properties in Lu-S compounds, resulting in the superconductivity and the band structures' nontriviality of LuS_2-*Cmca*. The predicted structures in LuS and Lu_2S_3 are the transition zone,

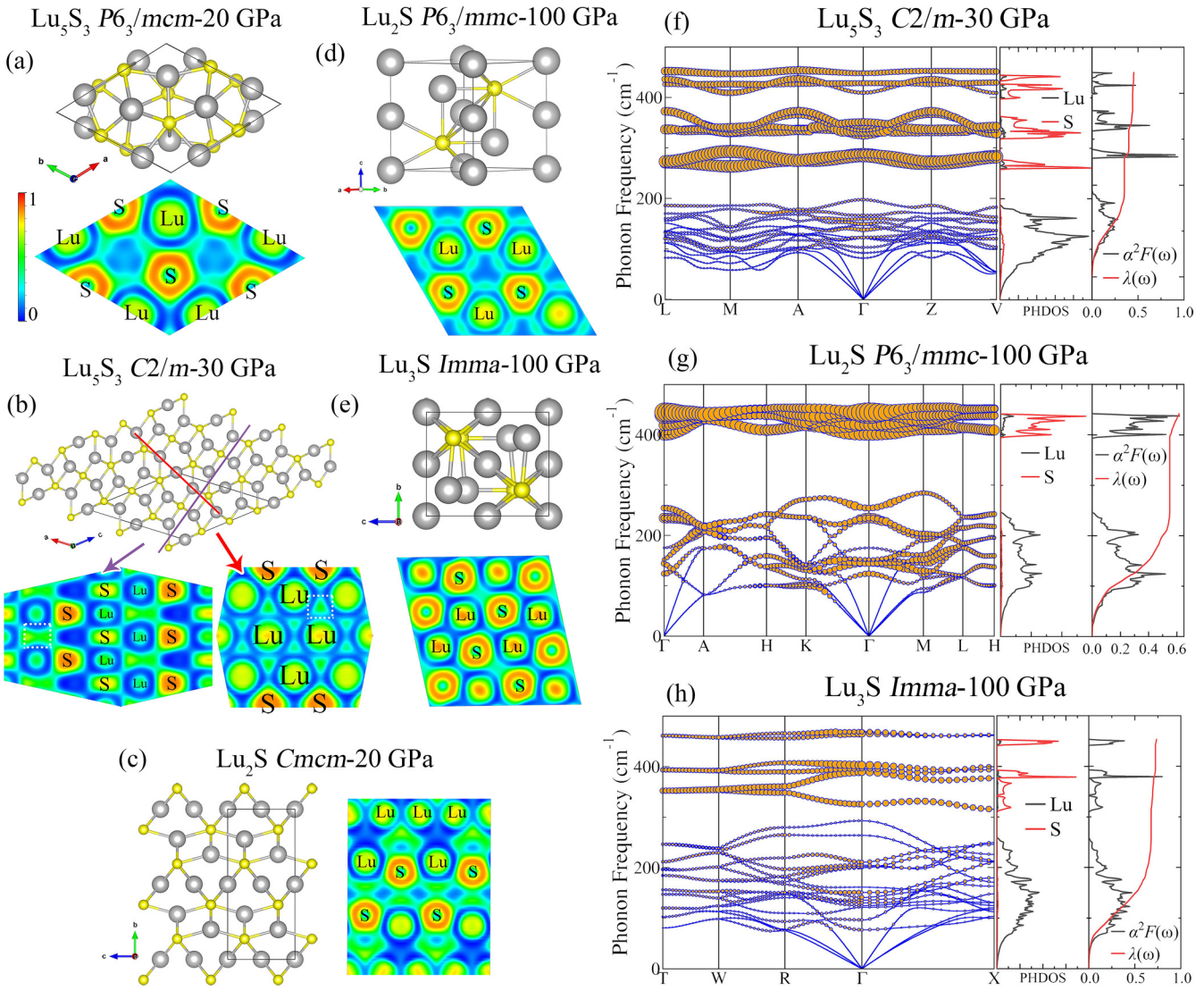

FIG. 8. (a)–(e) The crystal structure and corresponding ELF of the predicted structures Lu_5S_3-*C*2/*m*, Lu_5S_3-*P*6$_3$/*mcm*, Lu_2S-*Cmcm*, Lu_2S-*P*6$_3$/*mmc* and Lu_3S-*Imma*, under high pressures. The ELF in (b) shows the channel connecting S atoms in different planes. (f)–(h) The calculated phonon curves, PHDOS, the Eliashberg spectral function $\alpha^2F(\omega)$, and the electron-phonon integral $\lambda(\omega)$ of Lu_5S_3-*C*2/*m* at 30 GPa, Lu_2S-*P*6$_3$/*mmc* at 100 GPa, and Lu_3S-*Imma* at 100 GPa. The orange solid dots represent the phonon linewidth with the radii proportional to the strength.

in which Lu-*d* and S-*p* are comparable but the atoms are relatively isolated. In the Lu-rich compounds, Lu-*d* plays a chief role in the electronic structures, and the coupling between S atoms and Lu-*d* electrons acts as the key to the superconductivity, such as Lu_5S_3-*C*2/*m*, Lu_2S-*P*6$_3$/*mmc*, and Lu_3S-*Imma*.

IV. CONCLUSION

In summary, we explore the phase diagram of the Lu-S systems under high pressure combined with the machine learning graph theory accelerated structure searching and first-principles calculations. We predict 15 unique structures, encompassing seven exotic stoichiometries, all of which have the potential to be synthesized under high pressure. In the S-rich compounds, the S atoms' formation of cages is the key factor for the improvement of superconductivity, which is up to about 25 K for the metastable LuS_6-*C*2/*m* and LuS_6-*R*-3*m*, surpassing those of other binary metal sulfides. Lu-*d* electrons are more involved in the electronic properties in the predicted structures as the Lu/(Lu+S) ratio increases, and LuS_2-*Cmca* is both topologically nontrivial and superconducting. As for the Lu-rich compounds, the coupling between Lu-*d* electrons and S atoms become the crucial factor for superconductivity. Our work is helpful for understanding the transition metal sulfides under high pressure, providing some fundamental and unique insights for other metal sulfides in future experimental and theoretical works.

ACKNOWLEDGMENTS

This work was supported by the National Natural Science Foundation of China (Grants No. 52272265, No.

U1932217, No. 11974246, and No. 12004252), the National Key R&D Program of China (Grant No. 2018YFA0704300), and the Shanghai Science and Technology Plan (Grant No. 21DZ2260400).

[1] A. P. Drozdov, M. I. Eremets, I. A. Troyan, V. Ksenofontov, and S. I. Shylin, Conventional superconductivity at 203 kelvin at high pressures in the sulfur hydride system, Nature (London) **525**, 73 (2015).

[2] M. Einaga, M. Sakata, T. Ishikawa, K. Shimizu, M. I. Eremets, A. P. Drozdov, I. A. Troyan, N. Hirao, and Y. Ohishi, Crystal structure of the superconducting phase of sulfur hydride, Nat. Phys. **12**, 835 (2016).

[3] D. Duan, Y. Liu, F. Tian, D. Li, X. Huang, Z. Zhao, H. Yu, B. Liu, W. Tian, and T. Cui, Pressure-induced metallization of dense $(H_2S)_2H_2$ with high-T_c superconductivity, Sci. Rep. **4**, 6968 (2014).

[4] D. Duan, X. Huang, F. Tian, D. Li, H. Yu, Y. Liu, Y. Ma, B. Liu, and T. Cui, Pressure-induced decomposition of solid hydrogen sulfide, Phys. Rev. B **91**, 180502(R) (2015).

[5] N. W. Ashcroft, Hydrogen dominant metallic alloys: High temperature superconductors? Phys. Rev. Lett. **92**, 187002 (2004).

[6] H. Wang, J. S. Tse, K. Tanaka, T. Iitaka, and Y. Ma, Superconductive sodalite-like clathrate calcium hydride at high pressures, Proc. Natl. Acad. Sci. USA **109**, 6463 (2012).

[7] L. Ma, K. Wang, Y. Xie, X. Yang, Y. Wang, M. Zhou, H. Liu, X. Yu, Y. Zhao, H. Wang, G. Liu, and Y. Ma, High-temperature superconducting phase in clathrate calcium hydride CaH_6 up to 215 K at a pressure of 172 GPa, Phys. Rev. Lett. **128**, 167001 (2022).

[8] Y. Li, J. Hao, H. Liu, J. S. Tse, Y. Wang, and Y. Ma, Pressure-stabilized superconductive yttrium hydrides, Sci. Rep. **5**, 9948 (2015).

[9] H. Y. Liu, Naumov, R. Hoffmann, N. W. Ashcroft, and R. J. Hemley, Potential high-T_c superconducting lanthanum and yttrium hydrides at high pressure, Proc. Natl. Acad. Sci. USA **114**, 6990 (2017).

[10] F. Peng, Y. Sun, C. J. Pickard, R. J. Needs, Q. Wu, and Y. M. Ma, Hydrogen clathrate structures in rare earth hydrides at high pressures: Possible route to room-temperature superconductivity, Phys. Rev. Lett. **119**, 107001 (2017).

[11] I. A. Troyan, D. V. Semenok, A. G. Kvashnin, A. V. Sadakov, O. A. Sobolevskiy, V. M. Pudalov, A. G. Ivanova, V. B. Prakapenka, E. Greenberg, A. G. Gavriliuk, I. S. Lyubutin, V. V. Struzhkin, A. Bergara, I. Errea, R. Bianco, M. Calandra, F. Mauri, L. Monacelli, R. Akashi, and A. R. Oganov, Anomalous high-temperature superconductivity in YH_6, Adv. Mater. **33**, 2006832 (2021).

[12] Z. M. Geball, H. Liu, A. K. Mishra, M. Ahart, M. Somayazulu, Y. Meng, M. Baldini, and R. J. Hemley, Synthesis and stability of lanthanum superhydrides, Angew. Chem., Int. Ed. **57**, 688 (2018).

[13] M. Somayazulu, M. Ahart, A. K. Mishra, Z. M. Geballe, M. Baldini, Y. Meng, V. V. Struzhkin, and R. J. Hemley, Evidence for superconductivity above 260 K in lanthanum superhydride at megabar pressures, Phys. Rev. Lett. **122**, 027001 (2019).

[14] L. Boeri, R. Hennig, P. Hirschfeld, G. Profeta, A. Sanna, E. Zurek, W. E. Pickett, M. Amsler, R. Dias, M. I. Eremets, C. Heil, R. J. Hemley, H. Liu, Y. Ma, C. Pierleoni, A. N. Kolmogorov, N. Rybin, D. Novoselov, V. Anisimov, A. R. Oganov *et al.*, The 2021 room-temperature superconductivity roadmap, J. Phys.: Condens. Matter **34**, 183002 (2022).

[15] J. Nagamatsu, N. Nakagawa, T. Muranaka, Y. Zenitani, and J. Akimitsu, Superconductivity at 39 K in magnesium diboride, Nature (London) **410**, 63 (2001).

[16] C. Y. Pei, J. F. Zhang, Q. Wang, Y. Zhao, L. L. Gao, C. S. Gong, S. J. Tian, R. T. Luo, M. T. Li, W. G. Yang, Z. Y. Lu, H. C. Lei, K. Liu, and Y. P. Qi, Pressure-induced superconductivity at 32 K in MoB_2, Nat. Sci. Rev. **10**, nwad034 (2023).

[17] X. H. Liu, X. W. Huang, P. Song, C. Z. Wang, L. Y. Zhang, P. Lv, L. L. Liu, W. F. Zhang, J. H. Cho, and Y. Jia, Strong electron-phonon coupling superconductivity in compressed α-MoB_2 induced by double Van Hove singularities, Phys. Rev. B **106**, 064507 (2022).

[18] J. Lim, A. C. Hire, Y. Quan, J. S. Kim, S. R. Xie, S. Sinha, R. S. Kumar, D. Popov, C. Park, R. J. Hemley, Y. K. Vohra, J. J. Hamlin, R. G. Hennig, P. J. Hirschfeld, and G. R. Stewart, Creating superconductivity in WB_2 through pressure-induced metastable planar defects, Nat. Commun. **13**, 7901 (2022).

[19] C. Y. Pei, J. F. Zhang, C. S. Gong, Q. Wang, L. L. Gao, Y. Zhao, S. J. Tian, W. Z. Cao, C. H. Li, Z. Y. Lu, H. C. Lei, K. Liu, and Y. P. Qi, Distinct superconducting behaviors of pressurized WB_2 and ReB_2 with different local B layers, Sci. China: Phys., Mech. Astron. **65**, 287412 (2022).

[20] C. Kokail, C. Heil, and L. Boeri, Search for high-T_c conventional superconductivity at megabar pressures in the lithium-sulfur system, Phys. Rev. B **94**, 060502(R) (2016).

[21] Z. Zhao, S. Zhang, T. Yu, H. Xu, A. Bergara, and G. Yang, Predicted pressure-induced superconducting transition in electride Li_6P, Phys. Rev. Lett. **122**, 097002 (2019).

[22] Z. Liu, Q. Zhuang, F. Tian, D. Duan, H. Song, Z. Zhang, F. Li, H. Li, D. Li, and T. Cui, Proposed superconducting electride Li_6C by *sp*-hybridized cage states at moderate pressures, Phys. Rev. Lett. **127**, 157002 (2021).

[23] Z. S. Pereira, G. M. Faccin, and E. Z. da Silva, Predicted superconductivity in the electride Li_5C, J. Phys. Chem. C **125**, 8899 (2021).

[24] S. Kometani, M. I. Eremets, K. Shimizu, M. Kobayashi, and K. Amaya, Observation of pressure-induced superconductivity of sulfur, J. Phys. Soc. Jpn. **66**, 2564 (1997).

[25] V. V. Struzhkin, R. J. Hemley, H.-K. Mao, and Y. A. Timofeev, Superconductivity at 10–17 K in compressed sulphur, Nature (London) **390**, 382 (1997).

[26] E. Gregoryanz, V. V. Struzhkin, R. J. Hemley, M. I. Eremets, H. K. Mao, and Y. A. Timofeev, Superconductivity in the chalcogens up to multimegabar pressures, Phys. Rev. B **65**, 064504 (2002).

[27] K. Shimizu, Superconducting elements under high pressure, Phys. C (Amsterdam) **552**, 30 (2018).

[28] H. Zhang, W. Zhong, Y. Meng, B. Yue, X. Yu, J.-T. Wang, and F. Hong, Superconductivity above 12 K with possible multiband features in CsCl-type PbS, Phys. Rev. B **107**, 174502 (2023).

[29] Y. Fang, J. Pan, D. Zhang, D. Wang, H. T. Hirose, T. Terashima, S. Uji, Y. Yuan, W. Li, Z. Tian, J. Xue, Y. Ma, W. Zhao, Q. Xue, G. Mu, H. Zhang, and F. Huang, Discovery of superconductivity in 2*M* WS_2 with possible topological surface states, Adv. Mater. **31**, 1901942 (2019).

[30] Z. Chi, X. Chen, F. Yen, F. Peng, Y. Zhou, J. Zhu, Y. Zhang, X. Liu, C. Lin, S. Chu, Y. Li, J. Zhao, T. Kagayama, Y. Ma, and Z. Yang, Superconductivity in pristine 2H_a-MoS_2 at ultrahigh pressure, Phys. Rev. Lett. **120**, 037002 (2018).

[31] Q. Dong, J. Pan, S. Li, Y. Fang, T. Lin, S. Liu, B. Liu, Q. Li, F. Huang, and B. Liu, Record-high superconductivity in transition metal dichalcogenides emerged in compressed 2*H*-TaS_2, Adv. Mater. **34**, 2103168 (2021).

[32] J. M. Gonzalez, K. N. Cong, B. A. Steele, and I. I. Oleynik, Novel phases and superconductivity of tin sulfide compounds, J. Chem. Phys. **148**, 194701 (2018).

[33] R. Matsumoto, P. Song, S. Adachi, Y. Saito, H. Hara, A. Yamashita, K. Nakamura, S. Yamamoto, H. Tanaka, T. Irifune, H. Takeya, and Y. Takano, Pressure-induced superconductivity in tin sulfide, Phys. Rev. B **99**, 184502 (2019).

[34] S. Shao, W. Zhu, J. Lv, Y. Wang, Y. Chen, and Y. Ma, The exotically stoichiometric compounds in Al–S system under high pressure, npj Comput. Mater. **6**, 11 (2020).

[35] Y. Qi, Z. Xiao, J. Guo, H. Lei, T. Kamiya, and H. Hosono, Superconductivity in non-centrosymmetric sulfide Y_xS_4, EPL **121**, 57001 (2018).

[36] J. Chen, W. Cui, K. Gao, J. Hao, J. Shi, and Y. Li, Pressure-stabilized unconventional stoichiometric yttrium sulfides, Phys. Rev. Res. **2**, 043435 (2020).

[37] K. Gao, W. Cui, Q. Wang, J. Hao, J. Shi, S. Botti, M. A. L. Marques, and Y. Li, Superconductivity in S-rich phases of lanthanum sulfide under high pressure, Phys. Rev. Mater. **6**, 064801 (2022).

[38] K. Xia, H. Gao, C. Liu, J. Yuan, J. Sun, H. T. Wang, and D. Xing, A novel superhard tungsten nitride predicted by machine-learning accelerated crystal structure search, Sci. Bull. **63**, 817 (2018).

[39] H. Gao, J. Wang, Y. Han, and J. Sun, Enhancing crystal structure prediction by decomposition and evolution schemes based on graph theory, Fund. Res. **1**, 466 (2021).

[40] G. Kresse and J. Furthmüller, Efficient iterative schemes for *ab initio* total-energy calculations using a plane-wave basis set, Phys. Rev. B **54**, 11169 (1996).

[41] H. J. Monkhorst and J. D. Pack, Special points for Brillouin-zone integrations, Phys. Rev. B **13**, 5188 (1976).

[42] J. P. Perdew, K. Burke, and M. Ernzerhof, Generalized gradient approximation made simple, Phys. Rev. Lett. **77**, 3865 (1996).

[43] P. E. Blöchl, Projector augmented-wave method, Phys. Rev. B **50**, 17953 (1994).

[44] See Supplemental Material at http://link.aps.org/supplemental/10.1103/PhysRevResearch.6.023177 for the pseudopotential used to calculate electron-phonon properties; details of the relative enthalpy difference of the Lu-S binary compounds under high pressure; the phonon spectrum of the predicted Lu-S compounds under high pressure; the band structures and partial density of states of the predicted Lu-S compounds under high pressure; the sublattice of the predicted LuS_6 structures; the calculated structure parameters of the predicted Lu-S compounds under high pressure; and the k mesh and q mesh used for electron-phonon calculations.

[45] G. Pizzi, V. Vitale, R. Arita, S. Blügel, F. Freimuth, G. Géranton, M. Gibertini, D. Gresch, C. Johnson, T. Koretsune, J. Ibañez-Azpiroz, H. Lee, J.-M. Lihm, D. Marchand, A. Marrazzo, Y. Mokrousov, J. I. Mustafa, Y. Nohara, Y. Nomura, L. Paulatto *et al.*, WANNIER90 as a community code: New features and applications, J. Phys.: Condens. Matter **32**, 165902 (2020).

[46] Q. Wu, S. Zhang, H.-F. Song, M. Troyer, and A. A. Soluyanov, WANNIERTOOLS: An open-source software package for novel topological materials, Comput. Phys. Commun. **224**, 405 (2018).

[47] A. Togo and I. Tanaka, First principles phonon calculations in materials science, Scr. Mater. **108**, 1 (2015).

[48] P. Giannozzi, S. Baroni, N. Bonini, M. Calandra, R. Car, C. Cavazzoni, D. Ceresoli, G. L. Chiarotti, M. Cococcioni, I. Dabo, A. D. Corso, S. de Gironcoli, S. Fabris, G. Fratesi, R. Gebauer, U. Gerstmann, C. Gougoussis, A. Kokalj, M. Lazzeri, L. Martin-Samos *et al.*, QUANTUM ESPRESSO: A modular and open source software project for quantum simulations of materials, J. Phys.: Condens. Matter **21**, 395502 (2009).

[49] S. Baroni, S. de Gironcoli, A. Dal Corso, and P. Giannozzi, Phonons and related crystal properties from density-functional perturbation theory, Rev. Mod. Phys. **73**, 515 (2001).

[50] P. B. Allen and R. C. Dynes, Transition temperature of strong-coupled superconductors reanalyzed, Phys. Rev. B **12**, 905 (1975).

[51] G. N. Chesnut and Y. K. Vohra, Phase transformation in lutetium metal at 88 GPa, Phys. Rev. B **57**, 10221 (1998).

[52] E. F. OBannon, O. S. Pardo, P. Söderlind, D. Sneed, M. J. Lipp, C. Park, and Z. Jenei, Systematic structural study in praseodymium compressed in a neon pressure medium up to 185 GPa, Phys. Rev. B **105**, 144107 (2022).

[53] Y. Akahama, M. Kobayashi, and H. Kawamura, Structural studies of pressure-induced phase transitions in selenium up to 150 GPa, Phys. Rev. B **47**, 20 (1993).

[54] H. Fujihisa, Y. Akahama, H. Kawamura, H. Yamawaki, M. Sakashita, T. Yamada, K. Honda, and T. L. Bihan, Spiral chain structure of high pressure selenium-II′ and sulfur-II from powder x-ray diffraction, Phys. Rev. B **70**, 134106 (2004).

[55] O. Degtyareva, E. Gregoryanz, M. Somayazulu, H.-K. Mao, and R. J. Hemley, Crystal structure of the superconducting phases of S and Se, Phys. Rev. B **71**, 214104 (2005).

[56] H. Xiao, Y. Dan, B. Suo, and X. Chen, Comment on "Accelerated discovery of new 8-electron half-Heusler compounds as promising energy and topological quantum materials, J. Phys. Chem. C **124**, 2247 (2020).

[57] Y. An, J. Chen, Y. Yan, J. Wang, Y. Zhou, Z. Wang, C. Ma, T. Wang, R. Wu, and W. Liu, Higher-order topological and nodal superconducting transition-metal sulfides *M*S(M = Nb and Ta), Phys. Rev. B **108**, 054519 (2023).

[58] F. Hulliger and G. W. Hull, Superconductivity in rocksalt-type compounds, Solid State Commun. **8**, 1379 (1970).

[59] J. B. Gruber, R. Shaviv, E. F. Westrum Jr., R. Burriel, B. J. Beaudry, and P. E. Palmer, Thermophysical properties of the lanthanide sesquisulfides. IV. Schottky contributions, magnetic, and electronic properties of ε-phase Yb_2S_3 and Lu_2S_3, J. Chem. Phys. **98**, 1458 (1993).

[60] T. Seddik, F. Semari, R. Khenata, A. Bouhemadou, and B. Amrani, High pressure phase transition and elastic properties of lutetium chalcogenide, Phys. B **405**, 394 (2010).